

# A NETWORK OF SURFACE PRESSURE OBSERVATIONS TO CONSTRAIN AEROSOL FORCING IN MARS CLIMATE MODELS

R. J. Wilson, NASA Ames Research Center, Moffett Field CA, USA, (Robert.j.Wilson@nasa.gov), M.A. Kahre, NASA Ames Research Center, Moffett Field CA, USA.

**Introduction:** The evolving distribution of radiatively active dust and water ice clouds plays a major role in modulating the seasonal and interannual variation in the thermal forcing of the Martian atmosphere. Thermal tides are the global-scale atmospheric response to the diurnally varying thermal forcing due to aerosol heating within the atmosphere and radiative and convective heat transfer from the surface. The tide includes westward propagating (sun-synchronous) waves driven in response to solar heating, as well as nonmigrating waves that result from zonal variations in the thermotidal forcing caused by variations in topography and surface thermal properties and in the distribution of aerosols (dust and water ice clouds).

The migrating tides are of particular interest, since they are generally directly responsive to the aerosol distribution. However, distinguishing these tides from the mix of additional nonmigrating tides is difficult with only a limited number of surface observations. For example, Figure 1 shows the seasonal evolution of the amplitude of the diurnal ( $S_1$ ) and semidiurnal ( $S_2$ ) harmonics of surface pressure observed by the Rover Environmental Monitoring Station (REMS) aboard the MSL rover Curiosity in Gale crater (4.5°S, 137°E) for Mars Years 33 and 34. The figure highlights the very close correlation between the amplitude of  $S_2$  and the evolving global column dust opacity during the MY34 global dust storm. By contrast, the observed  $S_1$  response is less easily interpreted. It is surprisingly strong at the start of the regional dust storm at  $L_s = 323^\circ$  while the  $S_2$  response remains relatively weak, consistent with the global opacity.

It has become evident that radiative forcing by water ice clouds contributes significantly to the thermal balance particularly in the aphelion season, although details are still not well-constrained. Another poorly constrained aspect of aerosol forcing is the presence and impact of vertical variation of dust (detached dust layers) on thermal forcing. We suggest that a modest improvement in the spatial coverage of diurnally-resolved surface pressure can be an effective way of isolating tide modes that can be diagnostic of aerosol forcing in the Mars atmosphere.

The recent acquisition of surface pressure data by the Mars2020 mission in Jezero crater (18.5°N, 77.2°E) provides longitude coverage in the tropics, that complements the 5-year MSL record, the four-year record at Viking Lander 1 (VL1 at 22.5°N, 312°E), and the 1+year record at InSight (4.5°N,

135°E). The notable lack of interannual variability in Martian climate during the aphelion season ( $L_s=0-135^\circ$ ) allows these sets of lander data to be considered as a 4-station tropical network (Figure 2).

This presentation will describe an approach by which a global perspective of the evolving diurnal surface pressure response can be gained through the use of high-resolution Mars global climate model (MGCM) simulations. MGCMs include parameterizations that yield a thermal forcing field from distributions of dust and water ice clouds. Simulated atmospheric temperature and surface pressure are then obtained consistently as the model responds to the thermal forcing. The extent to which the simulated tide fields correspond to observations provides insight into how well the thermal forcing field is represented. A better understanding of the global and local scale influences on the diurnal variability of

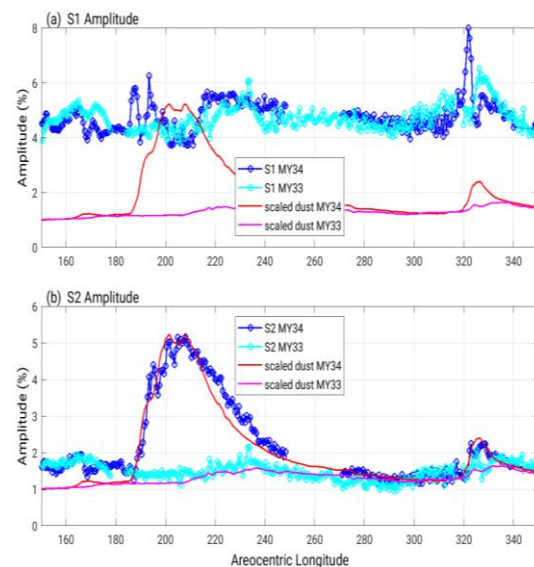


**Figure 1.** (a) The seasonal variation of the diurnal tide amplitude  $S_1$  at the MSL site for MY34 (blue) and MY33 (cyan). Amplitudes are normalized by the local diurnal-mean surface pressure. (b) As above but for the semidiurnal tide,  $S_2$  at the MSL site. The tropical (30°S-30°N) zonal-mean column dust visible opacity variations (from DGDM climatology) are shown as red and magenta lines for MY34 and MY33, respectively. The opacity has been scaled ( $\tau_{\text{scale}} = 0.9\tau + 0.75$ ) to emphasize the close correlation with  $S_2$ .

surface pressure is critical for detailed comparisons between atmospheric models and observations.

**Thermal Tides and Aerosol Forcing:** An observed tide harmonic,  $S_n$ , at a lander site

represents the sum over all zonal wavenumbers, including the corresponding migrating component and additional eastward and westward propagating nonmigrating components. Migrating tides include DW1, SW2, TW3, and QW4, respectively for the westward propagating diurnal, semidiurnal, terdiurnal, and quad-diurnal migrating tides. There is a roughly linear relationship between the SW2 amplitude and the dust column optical depth, which makes this mode an effective proxy for globally integrated thermal forcing. Moreover, due to the meridionally broad and vertically deep structure of the dominant Hough mode associated with SW2, the pressure response is relatively insensitive to the details of the vertical and latitude distribution of thermal forcing. By contrast, the surface pressure response of the migrating diurnal tide DW1 is weaker for a vertically extended dust distribution than for a more shallowly confined distribution with equivalent column optical depth. Thus, elevated dust layers or water ice clouds could have an influence on the observed  $S_1$  response.

The most prominent nonmigrating tides are the resonantly enhanced, eastward propagating diurnal and semidiurnal Kelvin waves, DE1 and SE2, with zonal wavenumbers 1 and 2, respectively. These waves are forced by zonal wave 2 and 4 components of thermal forcing, including the influence of topography and aerosol [Wilson and Hamilton, 1996]. Discussion of the influence of longitude variations of aerosol on DE1 is deferred to a later section.

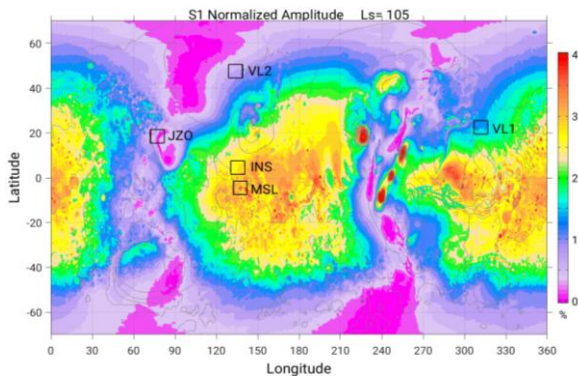


**Figure 2.** (a) The simulated spatial variation of normalized diurnal pressure variability,  $S_1$ , in % of diurnal-mean surface pressure for  $L_s = 105^\circ$ . The locations of MSL, InSight, Mars 2020, VL1 and VL2 are indicated. The prominent zonal wave 2 modulation is due to the interference between the westward (DW1) and eastward (DE1) diurnal tide components.

**MGCM Simulations:** We have been using a high-resolution version of the NASA Ames MGCM to simulate diurnal variability in surface pressure at scales ranging from that of Gale crater to the planetary scale, thus distinguishing the pressure signature of local topographically driven circulations from that of the global tide. The results from the predecessor GFDL version of the model are presented in Wilson *et al.* (2017). More recent simulations of the MSL

tides during the MY34 global dust storm are described in a manuscript in preparation.

The NASA Ames MGCM uses a finite volume dynamical core in a cubed-sphere geometry, which enables very high resolution simulations on a relatively uniform grid. The physics included in the MGCM are described in Kahre *et al.* (*this meeting*). Briefly, we include many options for the handling of dust and water ice clouds, including highly controlled prescriptions for their distributions and radiative effects. We have performed such simulations (C48 and C384) to examine the local and global-scale surface pressure responses. The C384 simulation has a resolution of  $0.25^\circ \times 0.25^\circ$  ( $\sim 15$  km). We have annual simulations at both resolutions. As we show below, the MGCM does reasonably well at capturing many of the tidal components discussed here.

The spatial distribution of normalized  $S_1$  amplitude at  $L_s = 105^\circ$  in a C384 simulation is shown in Figure 2. The large-scale response is dominated by a combination of DW1 and DE1, yielding the prominent zonal wave 2 modulation in diurnal tide amplitude. In the same season, there is a strong zonal wave 4 pattern in the  $S_2$  response (not shown), seen in previous simulation studies [Wilson and Hamilton, 1996; Guzewich *et al.*, 2016].

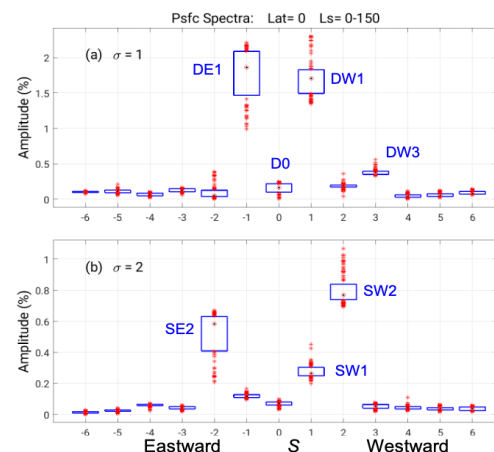


**Figure 3.** Box plots of equatorial tide mode amplitudes from the C384 simulation of the aphelion season derived from a space-time spectral analysis identifying eastward and westward propagating diurnal (a) and semidiurnal (b) components. The horizontal axis is zonal wavenumber. The vertical extent of the blue boxes spans the range of the middle two quartiles of amplitude in the  $L_s = 0-150^\circ$  season, while red stars represent the outlier values. The DW1/DE1 pair dominates the diurnal tide ( $S_1$ ) variability while the SW2/SE2 pair dominates the semidiurnal tide ( $S_2$ ) variability.

Figure 3 shows the results of a space-time analysis of the simulated equatorial surface pressure field, indicating the range of amplitudes of the eastward and westward propagating components of the equatorial diurnal and semidiurnal pressure fields in the  $L_s = 0-150^\circ$  season. It is evident that the dominant contributions to  $S_1$  structure and seasonal variability are associated with the DW1/DE1 pair of

tide modes, with smaller contributions from other waves, including DW2 and DW3. Similarly, the SW2/SE2 pair dominates the structure and variability of  $S_2$  in the aphelion season, with a lesser contribution from SW1. The meridional structures for both pairs of tide modes are quite broad so that changes in component amplitudes and phases would be reflected in similar tide changes throughout the tropics. MGCM simulations support the expectation that the migrating tide (SW2) accounts for the majority of the  $S_2$  response during dustier seasons.

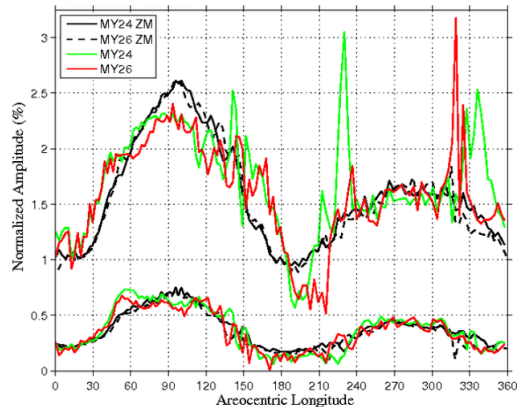


**Figure 4.** Simulations of DE1 and SE2 equatorial tide amplitudes with realistic dust scenarios for MY24 and MY26 (green and red, respectively). The black curves show results using zonally averaged dust

Figure 4 illustrates the sensitivity of the DE1 response to zonal variations in dust. Two simulations were carried out using the seasonally-varying but zonally averaged dust column scenarios for MY24 and MY26 compiled by *Montabone et al.* (2015). These yield nearly identical and smoothly varying seasonal variations in DE1 and SE1 in spite of the differing histories of regional dust storms in the two Mars years. The seasonal variation of the resonantly-enhanced Kelvin waves (DE1 and SE2) show a strong preference for the two solstice seasons, with a clear emphasis on the  $L_s = 90^\circ$  season. Re-running the simulations with the fully variable dust scenarios yields substantial variability in the DE1 response that is associated with changes to the zonal wave 2 distribution of column dust. These variations are particularly strong at the onset of the pre- and post-solstice regional storms. The 3 storm events associated with the Chyrse channel lead to significant amplification of DE1, while the Isidis flushing event at  $L_s=208^\circ$  in MY26 results in the phasing of the zonal wave-2 component of the dust pattern that suppresses the DE1 response. It is likely that rapid DE1 amplification is present at the start of the two MY34 dust storm events seen in Figure 1. There are also systematic, though weaker influences on the DE1 response in the aphelion season. While these simulations did not include water ice clouds, it is reasonable to anticipate that zonal variations in the tropical water ice cloud belt would induce changes as well.

**Aphelion Season Observations:** The amplitudes and phases of diurnal and semidiurnal pressure harmonics at the 4 network sites are shown in Figure 5. The synchronized decline and increase in  $S_2$  amplitude at VL1, INS, and MSL centered about  $L_s = 90^\circ$  is due to the destructive interference between SW2 and SE1 at the lander longitudes, separated by 180 degrees. By contrast,  $S_2$  at the longitude of Jezero crater has a relative maximum around solstice due to constructive interference between SW2 and SE2. Figure 6 shows a comparison of simulated and observed  $S_1$  amplitude. Similar comparisons can be made with the amplitudes and phases of  $S_2$  and higher order harmonics. The simulation also permits consideration of the constituent tide modes. In this simulation the model tends to overpredict the amplitude of  $S_1$ . This is attributed to an overly strong DW1 response, which likely is due to the absence of upper-level heating associated with radiatively active water ice clouds. The diurnal Kelvin wave (DE1) is also likely somewhat too strong, as suggested by the mismatch in amplitude (and phase, not shown) at Jezero crater. The simulation indicates that the difference in  $S_1$  amplitude between MSL and INS is largely due to the large-scale influence of the Mars dichotomy on DW1 and the local-scale influence of Gale crater; both enhance the response at MSL ( $4.5^\circ S$ ) vs InSight ( $4.5^\circ N$ ).

**Ongoing Research and Conclusions:** We are developing a fitting procedure where the network observations of the amplitudes and phases of  $S_1$  and  $S_2$  are used to estimate the evolving amplitudes and phases of DW1, DE1, SW2, and SE2 in the actual Mars atmosphere. We take advantage of the robustness of the predicted meridional structure of these key modes to be fitted, which enables a least-squares fit for their amplitude and phases as they evolve through the aphelion season. We have also been examining the sensitivity of the tide response to aspects of the aerosol forcing like the strength of the water ice cloud heating, and the vertical distribution of dust and water ice clouds. Thus, we anticipate that our estimates of the amplitudes of these diagnostic tide modes will provide useful guidance on assessing the radiative forcing by dust and water ice clouds.

## References

- Guzewich, S.D., et al. (2016), Atmospheric tides in Gale crater, *Icarus*, 268, 37-49,
- Kahre et al., (2022). 7<sup>th</sup> MAMO Conference, Paris, France. June 14-17, 2022.
- Montabone et al., (2015), Eight-year climatology of dust on Mars. *Icarus*.
- Wilson, R.J., and K.P. Hamilton (1996), Comprehensive model simulation of thermal tides in the martian atmosphere, *J. Atmos. Sci.* 53, 1290-1326.
- Wilson, R.J., J.M. Murphy, and D. Tyler (2017), Assessing atmospheric thermal forcing from surface pressure data; Separating thermal tides and local topographic influence Sixth International Workshop on the Mars At-

mosphere: Modeling and Observations, Granada, Spain, Jan 17-20, 2017. [http://www-mars.lmd.jussieu.fr/granada2017/abstracts/wilson\\_granada2017.pdf](http://www-mars.lmd.jussieu.fr/granada2017/abstracts/wilson_granada2017.pdf)

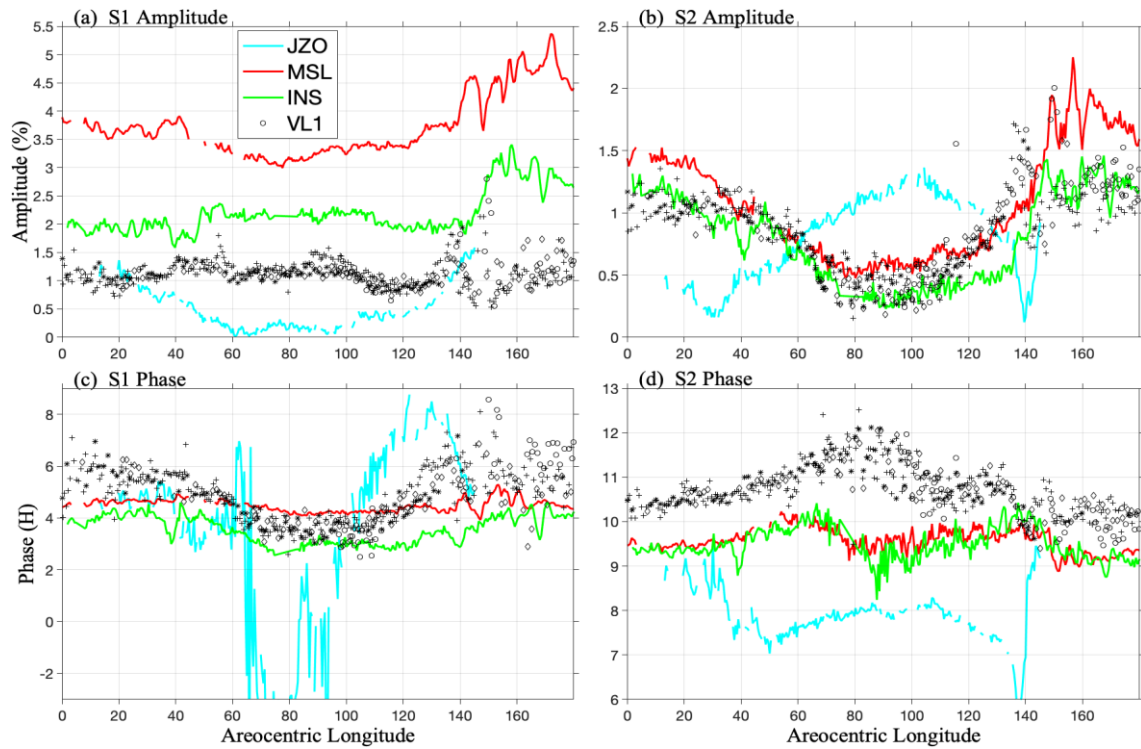


**Figure 5.** (a) Observations of the normalized diurnal harmonic amplitude of surface pressure,  $S_1$  at 4 sites on the Martian surface. These include Mars2020 (JZO, MY36, in cyan), MSL (MY33, in red), InSight (INS, green) and Viking Lander 1 (VL1, 4 years, in black) (b) Semidiurnal tide amplitude,  $S_2$ . (c) Diurnal tide phase. (d) Semidiurnal tide phase.

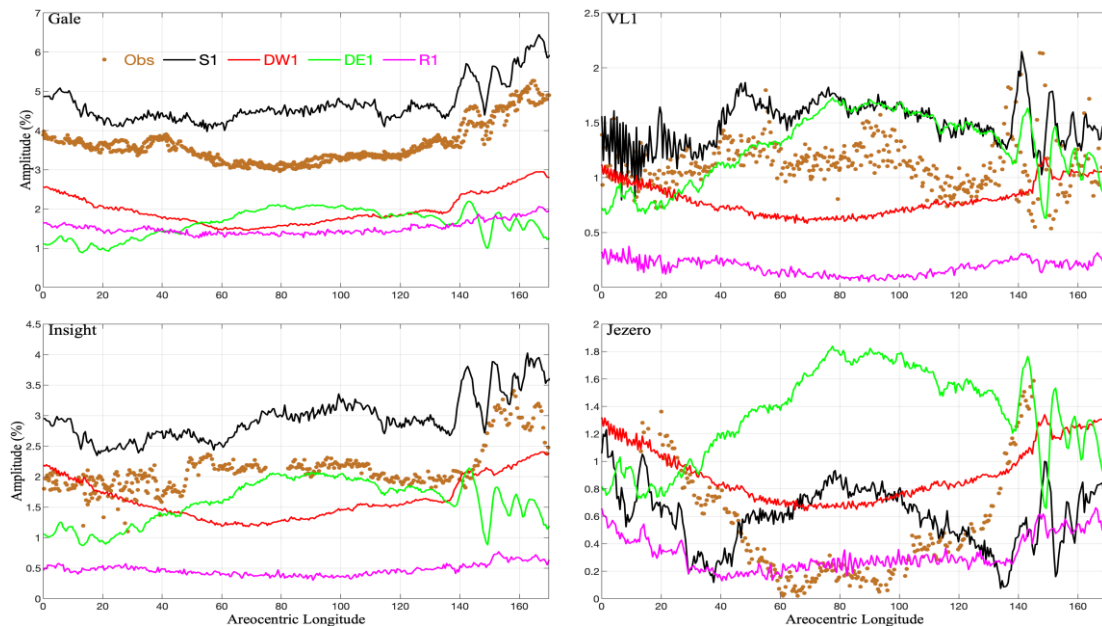


**Figure 6.** (a) Comparison of simulated  $S_1$  tide amplitude (black line) with observations by MSL in Gale crater (in brown). Also shown are the simulated seasonally-varying DW1 (red) and DE1 (green) amplitudes at the latitude of the lander. The magenta curve (R1) is the amplitude contribution attributed to the localized topographic response (as defined in *Wilson et al.* 2017). Note that wave phase need to be considered in combining wave component contribu-

